Real-Time Monitoring of Epithelial Cell-Cell and Cell-Substrate Interactions by Infrared Surface Plasmon Spectroscopy

Victor Yashunsky,[†*] Vladislav Lirtsman,[†] Michael Golosovsky,[†] Dan Davidov,[†] and Benjamin Aroeti[‡]
[†]The Racah Institute of Physics and [‡]Department of Cell and Developmental Biology, The Alexander Silberman Institute of Life Sciences, The Hebrew University of Jerusalem, Jerusalem, Israel

ABSTRACT The development of novel technologies capable of monitoring the dynamics of cell-cell and cell-substrate interactions in real time and a label-free manner is vital for gaining deeper insights into these most fundamental cellular processes. However, the label-free technologies available today provide only limited information on these processes. Here, we report a new (to our knowledge) infrared surface plasmon resonance (SPR)-based methodology that can resolve distinct phases of cell-cell and cell-substrate adhesion of polarized Madin Darby canine kidney epithelial cells. Due to the extended penetration depth of the infrared SP wave, the dynamics of cell adhesion can be detected with high accuracy and high temporal resolution. Analysis of the temporal variation of the SPR reflectivity spectrum revealed the existence of multiple phases in epithelial cell adhesion: initial contact of the cells with the substrate (cell deposition), cell spreading, formation of intercellular contacts, and subsequent generation of cell clusters. The final formation of a continuous cell monolayer could also be sensed. The SPR measurements were validated by optical microscopy imaging. However, in contrast to the SPR method, the optical analyses were laborious and less quantitative, and hence provided only limited information on the dynamics and phases of cell adhesion.

INTRODUCTION

The emergence of stimuli upon attachment of a cell to its neighboring cells and to extracellular substrates (e.g., the extracellular matrix) plays an important role in cell differentiation and tissue development. Epithelial cells have been extensively studied in this respect. A well-recognized example is simple epithelium, which forms a cell monolayer with barrier properties. These epithelial cells employ diverse means for contacting each other and the underlying extracellular matrix. Other examples include protein complexes and cytoskeletal elements that dynamically associate with specialized plasma membrane domains at the border between the apical and basolateral surfaces, which form tight and adherence junctions, and protein assemblies in the basal-lateral surfaces, which form desmosomal junctions and focal adhesions. These complex interactions, combined with the biochemical and physical characteristics of the extracellular matrix microenvironment, play a vital role in generating and maintaining epithelial cell polarity and epithelial tissue differentiation (1–6).

Conventional techniques for monitoring cell-substrate and cell-cell interactions typically involve fluorescent labeling of cells (7,8). However, the labeling procedures and the chemical modification introduced by the fluorescent probe can affect normal cell behavior (8). Thus, the development of sensitive label-free methodologies capable of tracking cell-substrate and cell-cell interactions in real time is crucial for ensuring reliable sensing of these important cellular processes. Several label-free techniques have been developed over the past few years to aid in the study of cell adhesion processes (9,10), including optical-based techniques such as optical waveguide spectroscopy (11–17), total internal reflection microscopy (18), reflectometric interference spectroscopy (19), surface plasmon resonance (SPR) (20–24), and infrared spectroscopy (25–28), and non-optical methods such as electrochemical impedance spectroscopy (29–31) and quartz crystal microbalance (32,33). However, most of these methodologies have been applied to the monitoring of cell-substrate rather than cell-cell adhesion since, the complexity of cell behavior precluded the detection of specific cell adhesion phases by these label-free methodologies (9–11).

Recently, we introduced the Fourier transform infrared (FTIR)-SPR method to obtain real-time and quantitative measurements of diverse dynamic processes that take place in living cells (34–36). In the study presented here, we combined what we believe is our novel FTIR-SPR method with conventional optical microscopy to monitor cell-cell and cell-substrate interactions. As a model cell system, we used the highly differentiated Madin Darby canine kidney (MDCK) epithelial cells. It is well recognized that these cells can exploit the indicated junctional complexes to form a highly polarized monolayer in vitro that faithfully mimics the biology of simple epithelium in vivo (6). Our main findings suggest that FTIR-SPR can quantitatively sense distinct phases in cell-substrate and cell-cell adhesion. The observed phases included cell sedimentation and attachment to the underlying substrate, and subsequent cell spreading and initiation of cell-cell contacts that eventually led to the formation of a continuous cell monolayer. We were able to detect these phases because of the unique ability of the FTIR-SPR method to produce an evanescent wave that penetrates deep (up to a few μm) into the cell layer, and the large propagation length

Submitted July 23, 2010, and accepted for publication October 12, 2010.

*Correspondence: victor.yashunsky@mail.huji.ac.il

Editor: Michael Edidin.

0006-3495/10/12/4028/9 $2.00

doi: 10.1016/j.bpj.2010.10.017

along the cell layer (up to ~70 μm, or a few cells). These physical characteristics enable sensitive monitoring of global changes in cell morphology that occur during cell-cell and cell-substrate interactions.

THEORY OF FTIR-SPR

Surface plasmon resonance

The surface plasmon (SP) is a surface electromagnetic wave that propagates along the metal-dielectric interface (x-direction) and decays in the z-direction, which is perpendicular to the interface. The SP is a transverse magnetic (TM) wave that can be resonantly excited by the light wave incident on the metal-dielectric interface using special couplers, such as prism or diffraction grating. The SPR appears as a sharp dip in the optical reflectivity spectrum. The position and depth of the SPR are extremely sensitive to the refractive index of the dielectric layer in contact with a metal that allows a highly sensitive refractometry. Currently, SPR biosensors are widely used to characterize the dynamics of molecular binding interactions, because the change in the refractive index occurs when molecules from a liquid sample bind to the metal surface coated with antibodies (37,38).

The most convenient way to excite the SP is to use Kretschmann's geometry (39), which employs the high-refractive index prism operating in the regime of attenuated total reflection (Fig. 1). The SP wave vector is determined by the complex dielectric permittivity of the analyte (i.e., the dielectric medium overlaying the metal) ε_d, and by the complex dielectric permittivity of the metal, ε_m. The components of the wave vector along the metal-dielectric interface and perpendicular to it are denoted as $k_{x,SP}$ and $k_{z,SP}$, respectively, and are given by the following expressions:

$$k_{x,SP} = k_0\left(\frac{\varepsilon_m\varepsilon_d}{\varepsilon_m + \varepsilon_d}\right)^{1/2}; |k_{z,SP}| = k_0\left(\frac{\varepsilon_d^2}{\varepsilon_m + \varepsilon_d}\right)^{1/2}, \quad (1)$$

where k_0 is the wave vector of the incident light. Because the real part of the ε_m is negative, $k_{z,SP}$ is imaginary in such a way that the SP wave is evanescent in the z-direction.

The SP wave vector in x-direction has real and imaginary parts, $k_{SP}=k_{SP}'+ik_{SP}''$. The resonance appears when the real part of k_{SP} matches k_x, the projection of the incident light wave vector along the direction of the SP propagation:

$$k_{SP}' = k_x = k_0 n_p \sin\theta_{SP}, \quad (2)$$

where n_p is the refractive index of the prism and θ_{SP} is the internal incident angle (Fig. 1). For fixed incident angle and wavelength interrogation, the SPR appears as a minimum in reflectivity at a certain wavelength λ_{min}, which is inexplicitly given by the following equation:

$$n_d(\lambda_{\min}) = \varepsilon_d^{1/2}(\lambda_{\min}) = n_p\sin\theta_{SP}\left(\frac{\varepsilon_m}{\varepsilon_m - n_p^2\sin^2\theta_{SP}}\right)^{1/2}. \quad (3)$$

Note that ε_p and ε_m depend on the wavelength; in particular, the real part of ε_m is a negative and is proportional to $1/\lambda^2$. The reflectivity in the vicinity of the SPR can be approximated by a Lorentzian (39,40):

$$R = |r_{mp}|^2\frac{1 - 4k_{SP}''\Gamma_{rad}}{\left(k_x - k_{SP}'\right)^2 + \left(k_{SP}'' + \Gamma_{rad}\right)^2}.$$

At resonance ($k_{SP}'= k_x$) the reflectivity achieves its minimal value

$$R_{\min} = \left|r_{mp}\frac{k_{SP}'' - \Gamma_{rad}}{k_{SP}'' + \Gamma_{rad}}\right|^2, \quad (4)$$

where r_{mp} is the Fresnel reflection coefficient at the prism-metal interface, k_{SP}'' is the lossy part of the SP wave vector, and Γ_{rad} is the radiation (coupling) loss that appears when the SP propagates along the thin metal film rather than along the bulk metal surface. For optimal coupling, which is achieved by a proper choice of the metal film thickness, $\Gamma = k_{SP}''$, and thus $R_{min} = 0$ (39,40).

Whereas conventional infrared spectroscopy traces spectral features related to the molecular absorption lines of the analyte, the FTIR-SPR technique uses spectroscopic information to identify the SPR wavelength with high precision. Because this wavelength is determined by the refractive

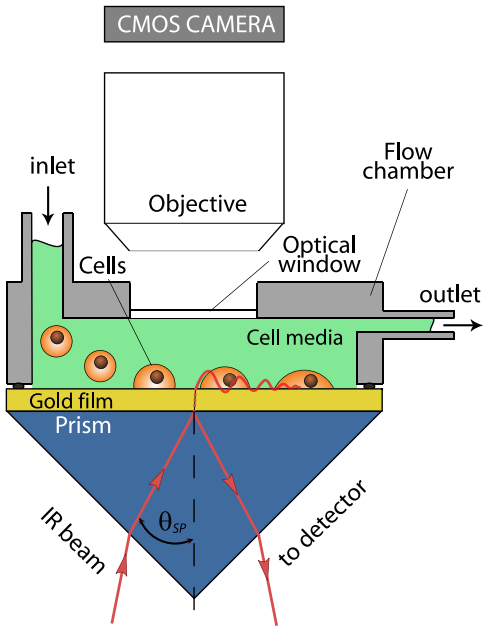

FIGURE 1 Experimental setup. A gold-coated prism is attached to a flow chamber filled with cell suspension in MEM-Hepes medium. The infrared SPR monitors the cell deposition process from the bottom side, i.e., through the substrate. A high-magnification zoom lens is used to observe the cell deposition.

index of the analyte (Eq. 3), the FTIR-SPR setup is in fact a highly sensitive refractometer. Tiny variations of the analyte refractive index (Δn_d) can be found from the shift of the SP resonance:

$$\Delta\lambda_{\min} = S\Delta n_d, \tag{5}$$

where $\Delta\lambda_{min}$ is the resonance wavelength shift and $S = \partial\lambda_{\min}/\partial n_d$ is the bulk sensitivity (34,37,40), which can be calculated analytically by differentiating Eq. 3 with respect to λ_{min}.

The SP wave is affected by changes in n_{eff} occurring in a thin layer in contact with the metal film. The thickness of this layer (i.e., the SPR penetration depth into the analyte layer (34,40)) is $\delta_z = 1/2k_{z,SP}$. Equation 1 yields

$$\delta_z = \mathrm{Im}\left[\frac{\lambda_{\min}}{4\pi n_d^2}\left(\varepsilon_m + n_d^2\right)^{1/2}\right]. \tag{6}$$

The penetration depth depends strongly on the wavelength; in particular, the penetration depth of the SP at the Au/water interface grows from $\delta_z = 0.3$ μm at λ~1 μm to $\delta_z = 10$ μm at λ~6 μm (34).

For an inhomogeneous medium whose properties vary in the z-direction (perpendicular to the direction of propagation of the SP wave), the refractive index of the analyte as it is sensed by the SPR is

$$n_{eff} = \frac{1}{\delta_z}\int_0^\infty n(z)\exp(-z/\delta_z)dz. \tag{7}$$

Cell-sensing by SPR

Living cells contain up to 30% organic substances, and their refractive index (n_{cell}) differs from that of a water-based medium (n_{med}) used to support cell growth. For a medium with cells, the effective refractive index sensed by the SP (Eq. 7) can be rewritten as

$$n_{eff} = n_{\mathrm{med}} + C_S\frac{1}{\delta_z}\int_0^\infty (n_{\mathrm{cell}} - n_{\mathrm{med}})A(z)\exp(-z/\delta_z)dz, \tag{8}$$

where $A(z)$ is the cross-section of the cell at height z above the substrate. During cell deposition and spreading, both A and C_S can change. If $A(z,t) = $ const., then Eq. 8 indicates that n_{eff} monitors the surface cell concentration on the substrate, C_S. Alternatively, if $C_S(t) = $ const., the SPR will sense the changes in cell morphology.

The spectral range of λ~2.5 μm is especially favorable for monitoring cell deposition and spreading. On the one hand, the SPR penetration depth (δ_z~2 μm) is lower than the cell's height, and hence the SPR senses only the cells that are in contact with the substrate, whereas the cells in solution are beyond the SP's probing range. On the other hand, the penetration depth of the SP is deep enough to sense a considerable volume of the cells deposited on the substrate. This is in contrast to the SP in the visible range, which has significantly smaller penetration depth ($\delta_z = 0.1$–0.3 μm) and therefore is sensitive mostly to the cell-substrate adhesion interface (40).

Cells not only affect the effective refractive index of the analyte but also introduce absorption and scattering of the SP wave. The imaginary part of the SP wave vector (k_{SP}'') includes both the absorption and scattering contributions: $k_{SP}'' = k_{abs}'' + k_{sc}''$. The absorption term reveals specific molecular spectroscopic information that in principle allows tracing of different cell constituents (e.g., proteins, lipids, polysaccharides, and water) (25–28), whereas the scattering term is sensitive to the cell's morphology.

Consequently, by measuring the resonant wavelength of the SPR, we determine the k_{SP}', which yields the cell coverage. On the other hand, the reflectivity at resonance measures the imaginary part of the SP wave vector (k_{SP}''; Eq. 4), and thus provides complementary information about the cell's morphology. In the following, we develop a semiquantitative model that relates to the reflectivity at SPR, R_{min}, to the cell shape and arrangement on the substrate.

Scattering of the SP wave

Visible light scattering can provide valuable information about cell shape and cell-cell attachment (41). Although scattering of evanescent waves (including SP) has been used in cell studies (12,15,16), the lack of adequate theoretical models has prevented the acquisition of quantitative information. Indeed, although SP wave scattering by subwavelength or one-dimensional defects has been intensively studied (42,43), to our knowledge, scattering by large and low-contrast objects such as cells on substrate ($r>>\lambda$, $\Delta n/n$~0.025) has not yet been studied theoretically.

In the absence of an appropriate theoretical model, we use the simplistic formalism based on Beer's law (44), which predicts exponential decay of the surface wave upon scattering: $I = I_0\exp(-k_{SP}''x)$, where

$$k_{SP}'' = C_S\Sigma_{SC} \tag{9}$$

Here C_S is the surface concentration of scattering objects, and Σ_{sc} is the scattering cross-section (for surface waves, Σ_{sc} has units of length). Measurements of evanescent wave scattering by large dielectric spheres ($r>>\lambda$) showed that the scattered light intensity scales with the sphere radius (45), i.e., Σ_{sc}~r. We assume that the Σ_{sc}~r relation holds for disk-shaped scatterers as well. Then Eq. 9 reduces to

$$\mathrm{k_{SP}''} = 2\pi\mathrm{rBC_S} = \mathrm{BP}, \tag{10}$$

where k''_{SP} is the imaginary part of the SP wave vector, $P = 2\pi rC_S$ is the total perimeter of scatterers per unit area, and the

(unknown) coefficient B is determined by the shape of the scatterer and by Δn, the dielectric contrast between the scatterer and the surrounding medium. This prompts the interesting conjecture that Eq. 10 is probably valid for a random assembly of sufficiently large uncorrelated weak scatterers of arbitrary shape, where P is the total length of scattering interfaces per unit area. In the context of cells and cell culture, this conjecture together with Eqs. 4 and 10 suggests that R_{min} measures the length of cell-medium interfaces per unit area.

MATERIALS AND METHODS

Cell culture

MDCK cells were cultured routinely as described previously (46). Cells were prepared for the SPR experiments as follows: MDCK cells of a confluent monolayer were detached from the dish by trypsinization (0.25% trypsin/EDTA in Puck's saline A; Biological Industries, Israel). The cells were then resuspended in 10 mL of modified Eagle's medium (MEM) Hanks' salts supplemented with 20 mM Hepes, pH 7.5 (MEM-Hepes). The suspended cells were immediately injected into the flow chamber of the FTIR-SPR setup (see Fig. 1).

FTIR-SPR setup

Our experimental setup is shown in Fig. 1. A right-angle ZnS prism (20 × 40 mm^2 base; ISP Optics, Irvington, NY) with a 20-nm-thick gold overlayer was attached to a 2 mL flow chamber filled with MEM-Hepes medium. The temperature of the flow chamber was stabilized at 37°C. The flow rate was controlled via a motorized bee syringe pump equipped with a variable speed controller. The prism-flow cell assembly was mounted on the vertical translation stage. The infrared SP was excited using Kretschmann's geometry as previously described (47). An FTIR device (Equinox 55, Bruker) was used as the broadband infrared source. The p-polarized infrared beam was collimated and reflected from the prism, and then focused onto a liquid-nitrogen-cooled MCT (HgCdTe) detector. Each FTIR spectrum lasted 25 s, representing an average over eight scans, with 8 cm^{-1} resolution. The s-polarized reflectivity spectrum was used as a background.

Experimental procedure

The prism was attached to the flow chamber of the FTIR setup and exposed to MEM-Hepes at 37°C for 1 h. The incident angle was set to $\theta_{SP} = 32.8°$ (Fig. 1). FTIR-SPR measurement started 15 min before cell suspension (~5 × 10^5 cells/mL) injection. The cell injection lasted 10 min at a rate of 200 μL/min, at which point it was stopped and replaced by a slow flow rate (25 μL/min) of cell-free MEM-Hepes medium. This step lasted for 260 min from initial cell sedimentation on the gold substrate to eventual formation of the cell monolayer. Finally, we pumped trypsin solution into the flow chamber at a flow rate of 200 μL/min during the first 2 min, and then slowed the rate down to 25 μL/min. The pumping at this slow flow rate continued for 15 min. Each experiment was repeated at least three times and yielded similar results.

Optical microscopy and image processing

Optical time-lapse images of cells cultured on the gold-coated prism surface were synchronized with the FTIR scans. Images were taken through a 0.5-mm-thick optical window by a CMOS camera (Lw 575; Lumenera) connected to the high magnification optical zoom lenses (NAVITAR 12X zoom) using a halogen-lamp upright coaxial illumination (Fig. 1). Fig. 2 *A* shows a representative section of the imaged field (0.5 × 10^{-2} mm^2).

The acquired images were processed with the use of ImageJ software (W. S. Rasband, ImageJ, National Institutes of Health, Bethesda, MD; http://rsb.info.nih.gov/ij/, 1997-2010), as follows: To determine the cell concentration on the Au surface (C_S) during cell injection (Fig. 2 *A*, stage *b*), a threshold filter was used to distinguish between the cells and the bare gold surface. The cell interior was then filled by means of a fill-hole procedure. In this way, the cell-covered area was distinguished from the cell-free area (Fig. 2 *B*, stage *b*). The fraction of the total image area covered by the cells yields the cell surface coverage, f, which is related to the surface cell concentration as $f = C_S A$, where A is the cell

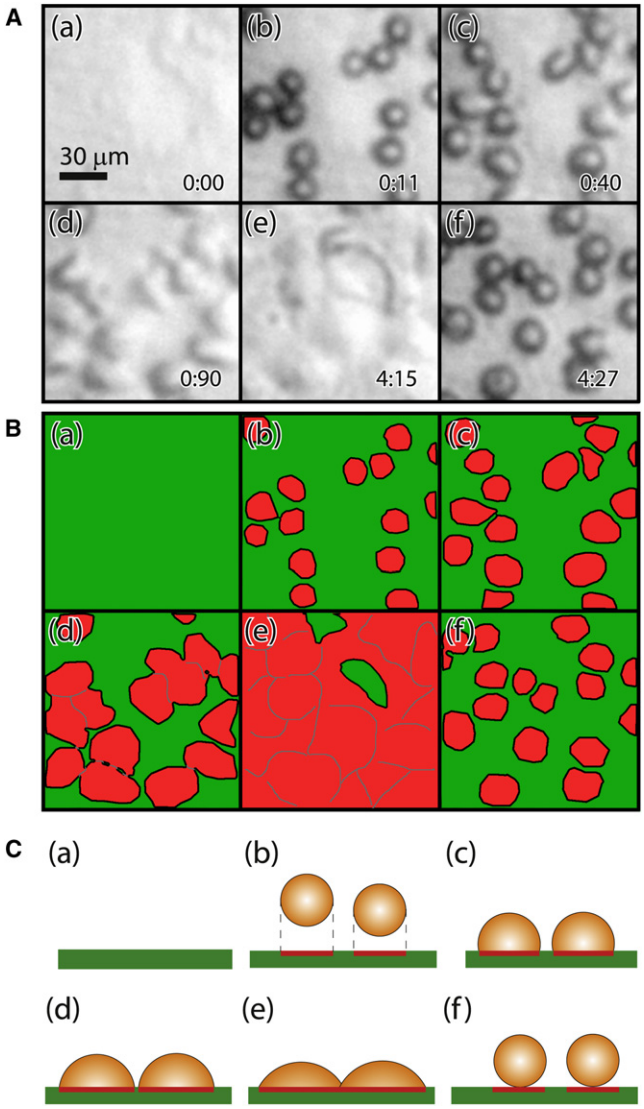

FIGURE 2 (*A*) Optical images of the gold-coated prism surface. All images were taken at the same location but at different times, and correspond to different phases of injection and spreading processes (*a*: bare gold; *b*: cell injection; *c*: cell spreading; *d*: cell-cell attachment; *e*: cell monolayer). Phase *f* corresponds to cell detachment after trypsin treatment. (*B*) Contour plots showing the cell coverage for the time moments indicated in panel *A*. Red color indicates cells (as projected from the top), and green color indicates the uncovered area. (*C*) Schematic description of different phases of cell injection and spreading (side view).

projection area. For spherical cells, $A=\pi r_0^2$, where r_0 is the radius of a cell in suspension. For later phases of cell spreading, when the cell projection deviates from the circle (Fig. 2 *B*, stages *c–e*), it is approximated by an ellipse, with semiaxes a and b in such a way that its area is $A = \pi ab$.

RESULTS

Cell injection and spreading analyzed by FTIR-SPR

Fig. 3 shows three representative infrared reflectivity curves in the SPR regime. In the absence of cells (*lower curve*, stage *a* in Fig. 2), the SPR appears as a sharp reflectivity minimum at $\nu_{min} = 4061$ cm^{-1} (this corresponds to $\lambda_{min} = 1/\nu_{min} = 2.46$ μm). After cell injection and spreading (*middle curve*, stages *b* and *c* in Fig. 2), this minimum is red-shifted toward 3920 cm^{-1}, indicating that the refractive index sensed by the SP (Eq. 8) has increased. During the cell-injection phase, the refractive index increment is associated with the growth of cell concentration (C_S), whereas during the cell-spreading phase it is associated with the growth of the projection area (A). In addition, the SPR dip becomes wider and shallower because the cells introduce scattering. Afterward, when the cells begin to form a continuous monolayer (*upper curve*, phases *d* and *e* in Fig. 2), the SPR is further red-shifted to 3850 cm^{-1} and becomes narrower. During these phases, the n_{eff} increases due to continuous growth of A and the associated increase in cell coverage (f), whereas the SPR narrows due to decreased scattering in the continuous cell monolayer. Moreover, an additional reflectivity minimum at 4170 cm^{-1} appears (Fig. 3, *boxed area*) at this stage. We attribute this minimum to the excitation of the guided TM_1 mode that propagates inside the cell layer. The appearance of this dip signifies the cell-cell attachment, since this waveguide mode can only propagate in a cluster consisting of several cells attached to one another. By analyzing the position (ν_{min}) and the depth (R_{min}) of the reflectivity minima associated with the SPR and the guided mode, we can draw quantitative conclusions about the cell layer morphology.

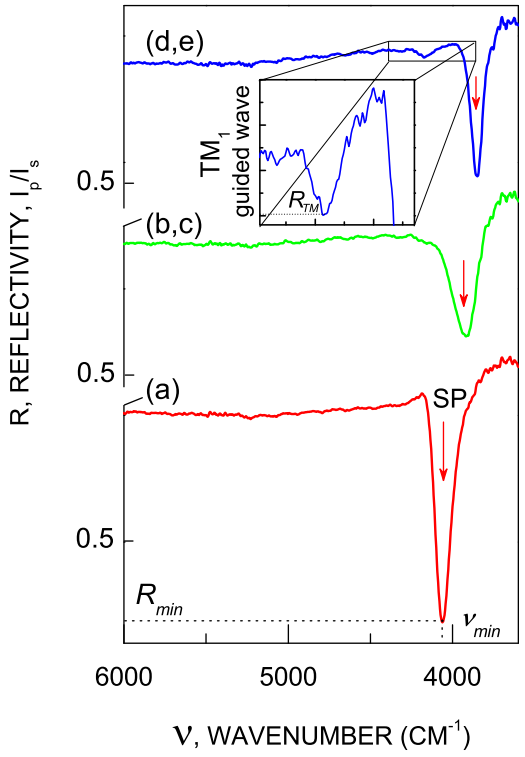

FIGURE 3 Infrared reflectivity spectra at different phases of cell deposition (see Fig. 2). The curves corresponding to each phase are vertically displaced for clarity. (*a*) Reflectivity from the ZnS/Au/medium interface before cell injection (background, $t = 0$). The sharp minimum at $\nu_{min} = 4061$ cm^{-1} corresponds to the SPR. (*b* and *c*) Reflectivity from the ZnS/Au/medium and cell interface (spreading phase, $t = 50$ min). The minimum corresponding to the SPR has been shifted to 3920 cm^{-1}. This shift is related to the presence of the cells. The minimum also became broader and shallower, indicating SP scattering on cells. (*d* and *e*) Reflectivity from the ZnS/Au/cell monolayer (monolayer phase, $t = 250$ min). The cell monolayer has been formed. The SPR minimum is further shifted to 3850 cm^{-1}. It also has become narrower and deeper, indicating decreased scattering in the cell monolayer. Note a small minimum at 4170 cm^{-1} (*boxed area*) that we attribute to the guided TM_1 mode in the cell monolayer.

Cell concentration and projected cell area are measured by the SPR shift

The SPR wavelength is sensitive to the surface cell concentration (C_S) and the lower portion of the cell body (see Theory of FTIR-SPR). In contrast to the visible SP wave that probes primarily the cell-substrate contacts ($\delta_z \leq 0.3$ μm at λ~0.6 μm), the deep penetration depth of the infrared SP ($\delta_z = 2$ μm at λ~2.5 μm) allows sensing of the cell area, which is almost the same as the projected cell area (A) measured by optical microscopy.

To evaluate C_S and A, we adopted the approach of Ramsden et al. (14), which they have developed in the context of an evanescent optical waveguide biosensing. The cell shape variation through the spreading phase is schematically depicted in Fig. 4 (*left to right*). While it is still in solution, the cell has a spherical shape with radius r_0. Upon cell spreading, the cell shape gradually changes from a full sphere to a spherical cap (curvature radius r, height $h < 2r$), whereas the cell volume V is preserved.

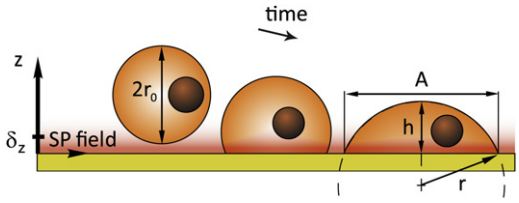

FIGURE 4 Schematic drawing of the cell shape during deposition. From left to right: spherical cells settle down onto the gold substrate (phase *b*; see Fig. 3) and then spread and become flat (phases *c–e*; see Fig. 3). The cell is approximated by the spherical cap with height h and the curvature radius r. The vertical axis on the left side schematically shows the evanescent field of the SP. The SP penetration depth δ_z is comparable to the cell height.

The cell height (above the substrate) is found from the following equation:

$$h^3 + 3hr^2 - \frac{6V}{\pi} = 0 \tag{11}$$

The cell cross-section at height z is

$$A(z) = \pi(h - z)(2r - h + z) \tag{12}$$

The projected cell area (the area of the contact region between the cell and the substrate) is found from Eq. 11 at $z = 0$:

$$A = \pi h\,(2r - h) \tag{13}$$

The cells were considered as spheres, ($r = r_0$, $h = 2r_0$) during the injection phase, whereas $r_0 = 10 \pm 1\ \mu m$ (measured by optical microscopy). The surface cell concentration (C_S) was found from the SPR measurements using Eqs. 8, and 12, and the refractive indices of the cell media and the cells. These were found in a separate SPR experiment: $n_{med} = 1.28$, $n_{cell} = 1.326$ at $\nu = 4425\ cm^{-1}$.

For the cell-spreading phase, we found A from Eqs. 8, 12, and 13, assuming that after the injection phase was over, the cell concentration remained unchanged ($C_S = C_0$; in other words, we neglected cell proliferation and cell death, which were minimal under our experimental conditions).

Fig. 5 shows the time-dependent alterations in C_S and A as derived from the SPR shift. It can be clearly seen that the cell projection area A increases with time. The increase is slower at the initial phase of cell spreading and faster at later times. After 180 min, A reaches a plateau at 840 μm^2 corresponding to surface coverage $f = C_S \times A = 0.92$. The projected area as measured by the SPR (*solid circles*) matches the direct optical microscopy measurements (*open squares*). Note, however, that the precision and time resolution of the SPR measurements are higher because it represents an average over 10^5 cells illuminated by the FTIR beam, whereas the optical microscopy averages only over a dozen cells. The inset shows that the C_S measured by the SPR and optical techniques are consistent as well.

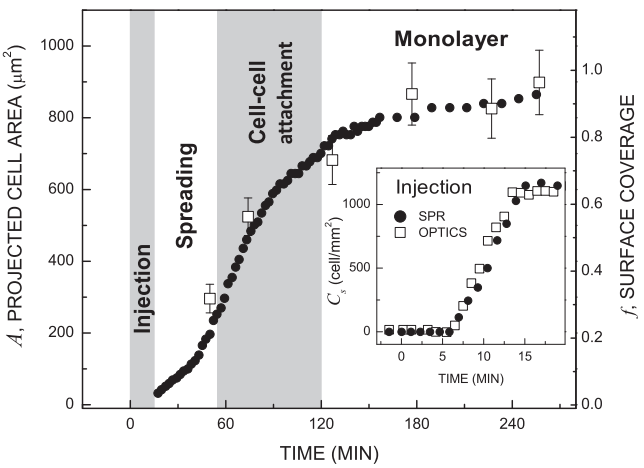

FIGURE 5 Time dependence of the projected cell area, A (*solid circles*), estimated from the SPR shift. Open squares show corresponding optical microscopy measurements. Note the good agreement. The inset shows surface cell concentration at the deposition phase as found from the SPR shift (*solid circles*) and optical microscopy (*open squares*). The different phases of cell spreading defined in the graph follow the notation of Fig. 2. The onset and duration of these phases were found from the SPR reflectivity.

The SPR depth/width monitors cell-cell attachment

Fig. 6, *c* and *b*, shows the time dependence of the SPR shift $\nu(t)$ and reflectivity $R_{min}(t)$. The $\nu(t)$ continuously grows with time, whereas the $R_{min}(t)$ achieves a maximum at

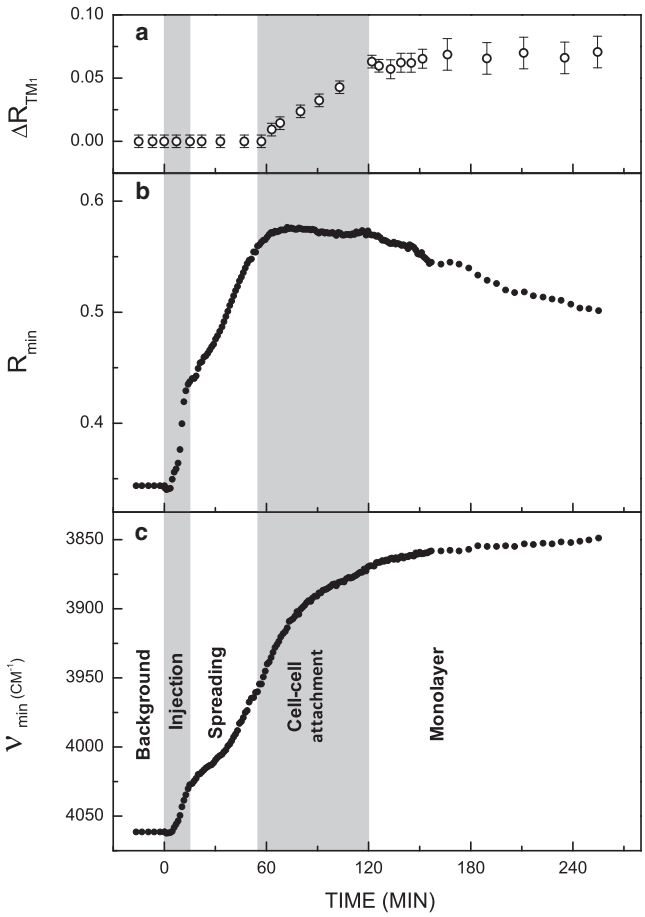

FIGURE 6 Time dependence of the SP position, ν_{min}, and depth, R_{min}, during cell deposition and spreading; $t = 0$ corresponds to cell injection. Lower panel: The SPR is continuously shifted, indicating an increase of the refractive index of the layer contacting the substrate. This is associated with cell deposition. Middle panel: The SP depth (which is determined by the scattering on cells) varies nonmonotonously through the cell deposition process. Upper panel: The magnitude of the reflectivity minimum is associated with the resonant excitation of the guided mode in the cell monolayer. This minimum characterizes the cell monolayer rather than individual cells. The SP and the guided-mode resonances characterize the cell-cell attachment for basal and apical cell sides, respectively.

$t = 60$ min and then decreases. Previous studies (11,15,16) that probed the spreading of living cells using an evanescent field of the optical waveguide observed a similar nonmonotonous time dependence of reflectivity, and attributed it to the different regimes of the evanescent wave scattering in the cell array. The information achieved so far from the scattering of evanescent waves (including SP) on cells has been mostly qualitative, due to the absence of appropriate theoretical models. Following the approach described by Cottier and Horvath (15) and Ramsden and Horvath (16), in this study we take the first steps, to our knowledge, to convert SP scattering into a quantitative tool to characterize cell spreading and cell-cell attachment.

Equations 4 and 10 suggest that the depth of the SPR, R_{min}, measures the length of cell-medium interfaces per unit area. Fig. 6 *b* shows that through the injection of cell suspension (t = 0–15 min), the R_{min} grows due to increasing C_S (whereas the cell shape does not change; see Fig. 2, stage *b*). When cells start to spread on the substrate (t = 15–55 min), the cell concentration remains unchanged (C_S = const). Then, the R_{min} grows mostly as a result of an increase in the cell perimeter, P (Eq. 10), arising from the expansion of individual cells on the substrate (Fig. 2, stage *c*).

When surface coverage achieves f~0.3 (at $t = 55$ min), the cells start to attach to each other (Fig. 2, stage *d*) and cell clusters appear. Here, f still increases. However, R_{min} grows much more slowly and even saturates, because the onset of cell-cell attachment is marked by the disappearance of cell-medium interfaces associated with scattering.

When the surface coverage reaches f~0.75 (at t = 120 min), the cells form a continuous monolayer with some cell-deficient voids (Fig. 2, stage *e*). Further cell spreading results in a gradual filling of these voids, in such a way that R_{min} decreases due to the disappearance of scattering interfaces. However, R_{min} does not regain its initial value even for the continuous monolayer, due to the proximity of the water absorption peak at 3400 cm^{-1}.

To characterize the varying cell morphology during the cell attachment process, we use the time excluding representation (Fig. 7). To this end, we plot $R_{min}(\nu_{min})$ dependences, in similarity to previous studies (11,15,16). Since ν_{min} measures surface coverage, f, whereas $R_{min,}$ measures the length of cell-medium interfaces per unit area, P (Eq. 10), the $R_{min}(\nu_{min})$ dependence mimics the $P(f)$ dependence. The latter is well known in the context of thin-film growth (48) and has been used to characterize morphological changes during film deposition. Indeed, Fig. 7 clearly shows the different phases of cell-substrate and cell-cell interactions: individual cell spreading, development of cell clusters, and formation of a continuous monolayer. It is noteworthy that the $R_{min}(\nu_{min})$ dependences for the direct process (cell attachment; *black symbols*) and the reverse process (cell detachment after trypsinization; *red symbols*) almost coincide, although the latter process is much faster than the former.

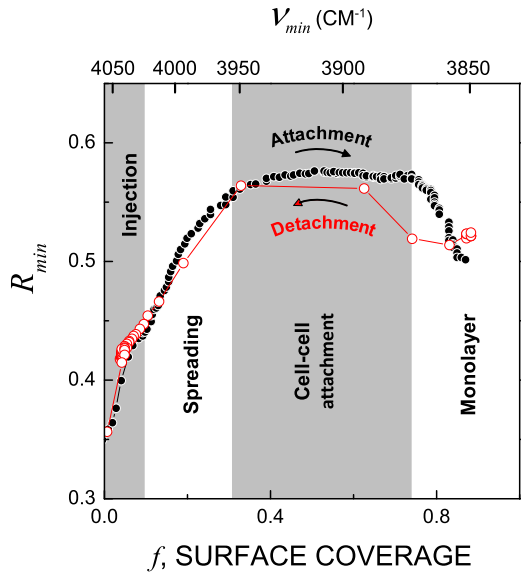

FIGURE 7 Dependence of R_{min} on surface coverage f (estimated from ν_{min}) during cell deposition (*solid circles*) and detachment after trypsinization (*open circles*). Although the rates of these two processes are very different, the $R_{min}(f)$ dependences are almost identical, indicating that upon detachment the cells pass through essentially the same stages as upon spreading, but in reverse order.

Cell-cell attachment revealed by the appearance of a guided mode

Additional evidence that allows one to pinpoint the onset of cell-cell-attachment comes from the kinetics of the guided mode resonance in the cell monolayer, which results in an additional reflectivity dip apart from that associated with the SPR (see Fig. 3, *boxed area*). Indeed, the cell monolayer between the metal substrate and growth medium can be considered as a very imperfect planar optical waveguide. The cutoff condition for the TM_1 mode excitation there is $k_0 h(n_{cell}^2 - n_{med}^2)^{1/2} = \pi/2$ (34), where h is the height of the waveguide and k_0 is the wave vector of the incident light wave. To excite this mode effectively, the interaction between the incident electromagnetic wave and the guided optical wave must be sufficiently long. An individual cell is not large enough to allow guided-mode excitation; therefore, to excite this guided wave, a cluster containing several cells is required.

Fig. 6 *a* shows how the magnitude of the guided-mode resonance varies during cell spreading. The guided-mode resonance is absent during cell injection and initial spreading. It appears only at $t_1 = 55$ min. The magnitude of the guided-mode resonance increases with time and achieves saturation after $t_2 = 120$ min. We attribute t_1 to the onset of cell-cell attachment, and t_2 to the completion of the cell monolayer.

Although the cell-cell attachment and monolayer formation can be traced indirectly through the measurement of R_{min} and ν_{min} (Fig. 6, *b* and *c*), the guided-mode resonance

monitors the cell-cell attachment directly and allows precise timing of its onset.

DISCUSSION

FTIR-SPR versus other label-free techniques

In this work we demonstrate the ability of FTIR-SPR to measure quantitatively and with high temporal resolution the different phases of cell adhesion, i.e., initial cell-substrate attachment, cell spreading, cell clustering, and subsequent formation of an epithelial cell layer. The ability of the FTIR-SPR method to resolve these phases stems from two features of the infrared SP: 1), the extended penetration depth into the cell body/layer (up to 2 μm), which permits sensitive probing of the degree of cell coverage (f) on the substrate; and 2), the pronounced lateral propagation length of the infrared SP (~70 μm). These features allow reconstruction of the cell shape and cell organization on the substrate from the SP shift and scattering, as derived from the SPR depth (R_{min}). In visible-wavelength-based techniques (e.g., optical waveguide spectroscopy and SPR), these two parameters are considerably smaller (penetration depth is normally < 0.3 μm (11), and in the case of SPR the propagation length extends only to ~2 μm (40)). Hence, the sensitivity of these methodologies is confined mainly to the cell-substrate interface. In contrast, the FTIR-SPR method is sensitive not only to the cell-substrate contacts but also to large portions of the cell body, thus allowing the detection of changes in cell shape as well as processes related to intercellular communication processes (e.g., cell-cell attachment and cell monolayer formation).

Other nonoptical, label-free methods, such as electrochemical impedance spectroscopy and quartz crystal microbalance, have been used to study cell adhesion (31). However, although these methods can sense the dynamics of cell adhesion, they typically cannot relate the measured parameters to specific changes in cell morphology and substrate coverage.

FTIR-SPR versus optical microscopy

In principle, cell-substrate and cell-cell adhesion phases can be quantitatively evaluated by various types of optical microscopy, including fluorescence and phase contrast/reflection microscopy (18). However, the FTIR-SPR method provides several significant advantages. Whereas optical microscopy can normally examine relatively small cell numbers (from a single cell up to a few hundreds of cells), FTIR-SPR measures simultaneously the behavior of $>10^5$ cells. Thus, the FTIR-SPR approach could be superior to microscopy-based techniques because it allows cell adhesion processes to be studied quantitatively over large cell populations. Second, the sensitive detection of steps in cell-substrate and cell-cell adhesion would require the application of several optical microscopy-based approaches (e.g., total internal reflection fluorescence microscopy would sensitively detect cell-substrate but not cell-cell attachments, and conventional and confocal laser scanning fluorescence microscopy would sense mainly cell-cell adhesion). Here we show that the FTIR-SPR method is capable of sensitively and simultaneously detecting cell-substrate and cell-cell attachment.

CONCLUSIONS

Using FTIR-SPR, we demonstrated the existence of multiple phases in cell-substrate and cell-cell interactions of epithelial cells. Remarkably, the FTIR-SPR method was able to measure the dynamic occurrence of these phases in real time, with high sensitivity and in a label-free manner. We predict that our current development of FTIR-SPR will serve as a powerful new experimental strategy for studying cell adhesion processes in health and disease.

We thank Dr. Boaz Ran and Dr. Tsafrir Bravman (Bio-Rad, Haifa, Israel) for constant encouragement and stimulating discussions, and Prof. A. A. Maradudin for discussions about SP scattering.

This research was supported by the Israeli Ministry of Industry and Trade through the Nofar program.

REFERENCES

1. Gumbiner, B. M. 1996. Cell adhesion: the molecular basis of tissue architecture and morphogenesis. *Cell.* 84:345–357.
2. Nelson, W. J. 2003. Adaptation of core mechanisms to generate cell polarity. *Nature.* 422:766–774.
3. Ingber, D. E. 2003. Tensegrity II. How structural networks influence cellular information processing networks. *J. Cell Sci.* 116:1397–1408.
4. Bershadsky, A. D., N. Q. Balaban, and B. Geiger. 2003. Adhesion-dependent cell mechanosensitivity. *Annu. Rev. Cell Dev. Biol.* 19:677–695.
5. Engler, A. J., S. Sen, …, D. E. Discher. 2006. Matrix elasticity directs stem cell lineage specification. *Cell.* 126:677–689.
6. Bryant, D. M., and K. E. Mostov. 2008. From cells to organs: building polarized tissue. *Nat. Rev. Mol. Cell Biol.* 9:887–901.
7. Axelrod, D. 2008. Chapter 7: Total internal reflection fluorescence microscopy. *Methods Cell Biol.* 89:169–221.
8. Wang, Y. X., J. Y. J. Shyy, and S. Chien. 2008. Fluorescence proteins, live-cell imaging, and mechanobiology: seeing is believing. *Annu. Rev. Biomed. Eng.* 10:1–38.
9. Cooper, M. A. 2006. Non-optical screening platforms: the next wave in label-free screening? *Drug Discov. Today.* 11:1068–1074.
10. Marcotte, L., and A. Tabrizian. 2008. Sensing surfaces: challenges in studying the cell adhesion process and the cell adhesion forces on biomaterials. *IRBM.* 29:77–88.
11. Fang, Y., A. M. Ferrie, …, J. Balakrishnan. 2006. Resonant waveguide grating biosensor for living cell sensing. *Biophys. J.* 91: 1925–1940.
12. Horvath, R., K. Cottier, …, J. J. Ramsden. 2008. Multidepth screening of living cells using optical waveguides. *Biosens. Bioelectron.* 24: 805–810.
13. Hug, T. S., J. E. Prenosil, and M. Morbidelli. 2001. Optical waveguide lightmode spectroscopy as a new method to study adhesion of anchorage-dependent cells as an indicator of metabolic state. *Biosens. Bioelectron.* 16:865–874.

14. Ramsden, J. J., S. Y. Li, …, J. E. Prenosil. 1995. Optical method for measurement of number and shape of attached cells in real time. *Cytometry.* 19:97–102.

15. Cottier, K., and R. Horvath. 2008. Imageless microscopy of surface patterns using optical waveguides. *Appl. Phys. B.* 91:319–327.

16. Ramsden, J. J., and R. Horvath. 2009. Optical biosensors for cell adhesion. *J. Recept. Signal Transduct. Res.* 29:211–223.

17. Aref, A., R. Horvath, …, J. J. Ramsden. 2009. Optical monitoring of stem cell-substratum interactions. *J. Biomed. Opt.* 14:010501.

18. Axelrod, D., and G. M. Omann. 2006. Combinatorial microscopy. *Nat. Rev. Mol. Cell Biol.* 7:944–952.

19. Möhrle, B. P., K. Köhler, …, G. Gauglitz. 2006. Label-free characterization of cell adhesion using reflectometric interference spectroscopy (RIfS). *Anal. Bioanal. Chem.* 384:407–413.

20. Chabot, V., C. M. Cuerrier, …, P. G. Charette. 2009. Biosensing based on surface plasmon resonance and living cells. *Biosens. Bioelectron.* 24:1667–1673.

21. Cuerrier, C. M., V. Chabot, …, M. Grandbois. 2008. Surface plasmon resonance monitoring of cell monolayer integrity: implication of signaling pathways involved in actin-driven morphological remodeling. *Cell. Mol. Bioeng.* 1:229–239.

22. Hide, M., T. Tsutsui, …, K. Yoshizato. 2002. Real-time analysis of ligand-induced cell surface and intracellular reactions of living mast cells using a surface plasmon resonance-based biosensor. *Anal. Biochem.* 302:28–37.

23. Yanase, Y., H. Suzuki, …, M. Hide. 2007. The SPR signal in living cells reflects changes other than the area of adhesion and the formation of cell constructions. *Biosens. Bioelectron.* 22:1081–1086.

24. Peterson, A. W., M. Halter, …, A. L. Plant. 2009. Surface plasmon resonance imaging of cells and surface-associated fibronectin. *BMC Cell Biol.* 10:16.

25. Jamin, N., P. Dumas, …, G. P. Williams. 1998. Highly resolved chemical imaging of living cells by using synchrotron infrared microspectrometry. *Proc. Natl. Acad. Sci. USA.* 95:4837–4840.

26. Raichlin, Y., and A. Katzir. 2008. Fiber-optic evanescent wave spectroscopy in the middle infrared. *Appl. Spectrosc.* 62:55A–72A.

27. Yamaguchi, R., A. Hirano-Iwata, …, H. Miyazaki. 2009. In situ real-time monitoring of apoptosis on leukemia cells by surface infrared spectroscopy. *J. Appl. Phys.* 105:203902.

28. Zelig, U., J. Kapelushnik, …, I. Nathan. 2009. Diagnosis of cell death by means of infrared spectroscopy. *Biophys. J.* 97:2107–2114.

29. Giaever, I., and C. R. Keese. 1993. A morphological biosensor for mammalian cells. *Nature.* 366:591–592.

30. Atienza, J. M., N. C. Yu, …, Y. A. Abassi. 2006. Dynamic and label-free cell-based assays using the real-time cell electronic sensing system. *Assay Drug Dev. Technol.* 4:597–607.

31. Xiao, C., B. Lachance, …, J. H. Luong. 2002. An in-depth analysis of electric cell-substrate impedance sensing to study the attachment and spreading of mammalian cells. *Anal. Chem.* 74:1333–1339.

32. Heitmann, V., and J. Wegener. 2007. Monitoring cell adhesion by piezoresonators: impact of increasing oscillation amplitudes. *Anal. Chem.* 79:3392–3400.

33. Fredriksson, C., S. Kihlman, …, B. Kasemo. 1998. The piezoelectric quartz crystal mass and dissipation sensor: A means of studying cell adhesion. *Langmuir.* 14:248–251.

34. Golosovsky, M., V. Lirtsman, …, B. Aroeti. 2009. Midinfrared surface-plasmon resonance: a novel biophysical tool for studying living cells. *J. Appl. Phys.* 105:1020–1021.

35. Ziblat, R., V. Lirtsman, …, B. Aroeti. 2006. Infrared surface plasmon resonance: a novel tool for real time sensing of variations in living cells. *Biophys. J.* 91:776–776.

36. Yashunsky, V., S. Shimron, …, B. Aroeti. 2009. Real-time monitoring of transferrin-induced endocytic vesicle formation by mid-infrared surface plasmon resonance. *Biophys. J.* 97:1003–1012.

37. Homola, J. 2003. Present and future of surface plasmon resonance biosensors. *Anal. Bioanal. Chem.* 377:528–539.

38. Bronner, V., G. Denkberg, …, T. Bravman. 2010. Therapeutic antibodies: discovery and development using the ProteOn XPR36 biosensor interaction array system. *Anal. Biochem.* 406:147–156.

39. Raether, H. 1988. Surface Plasmons on Smooth and Rough Surfaces and on Gratings. Springer-Verlag, Berlin/New York.

40. Johansen, K., H. Arwin, …, B. Liedberg. 2000. Imaging surface plasmon resonance sensor based on multiple wavelengths: Sensitivity considerations. *Rev. Sci. Instrum.* 71:3530–3538.

41. Srinivas, S. P., J. A. Bonanno, …, W. Van Driessche. 2003. Measurement of rapid changes in cell volume by forward light scattering. *Pflugers Arch.* 447:97–108.

42. Leskova, T. A., A. A. Maradudin, and I. V. Novikov. 2000. Scattering of light from the random interface between two dielectric media with low contrast. *JOSA A.* 17:1288–1300.

43. Pincemin, F., A. A. Maradudin, …, J. Greffet. 1994. Scattering of a surface plasmon polariton by a surface defect. *Phys. Rev. B.* 50:15261–15275.

44. Chou, T., and D. R. Nelson. 1994. Surface-wave scattering at nonuniform fluid interfaces. *J. Chem. Phys.* 101:9022–9032.

45. Prieve, D. C., and J. Y. Walz. 1993. Scattering of an evanescent surface wave by a microscopic dielectric sphere. *Appl. Opt.* 32:1629–1641.

46. Sason, H., M. Milgrom, …, B. Aroeti. 2009. Enteropathogenic *Escherichia coli* subverts phosphatidylinositol 4,5-bisphosphate and phosphatidylinositol 3,4,5-trisphosphate upon epithelial cell infection. *Mol. Biol. Cell.* 20:544–555.

47. Lirtsman, V., M. Golosovsky, and D. Davidov. 2008. Infrared surface plasmon resonance technique for biological studies. *J. Appl. Phys.* 103:014702.

48. Tomellini, M., and M. Fanfoni. 2006. Mean field approach for describing thin film morphology. *J. Phys. Condens. Matter.* 18:4219–4230.